WHERE THE SONAR EQUATION FEARS TO TREAD

Derek R. Olson Applied Research Lab, Pennsylvania State University, State College, PA
Daniel C. Brown Applied Research Lab, Pennsylvania State University, State College, PA
Charles W. Holland Applied Research Lab, Pennsylvania State University, State College, PA
Cale F. Brownstead Applied Research Lab, Pennsylvania State University, State College, PA

1 INTRODUCTION

The scattering cross section characterizes the scattering properties of a rough interface or heterogeneous volume in a manner that is independent of measurement system and geometry [1]. As such it is defined for incident and scattered plane waves of a single frequency. However, any measurement system with finite resolution, either in the range or azimuthal directions, will result in an estimate of the cross section that is averaged over finite frequency, azimuthal and grazing angle intervals. For many experimental geometries, such as those set up to measure the interface scattering cross section at low grazing angles, the frequency and azimuthal averaging are insignificant because the incident field is well-approximated by a plane wave, and the scattering cross section varies slowly within the ensonified region [1] [2]. Under these conditions, the scattering cross section may be estimated from averaged reverberation intensity using the sonar equation, and it may be assumed that a one-to-one mapping exists between time and grazing angle.

However, for certain geometries, such as interface scattering near the specular direction of a rough interface, or volume scattering for normal-incidence systems, plane-wave incidence is a poor approximation of the incident field, and the curvature must be taken into account in scattering strength estimates. For cases in which the scattering cross section varies rapidly as a function of grazing angle within the ensonfified region, use of the sonar equation will result in a biased or distorted estimate of the scattering cross section [3]. Essentially, several terms in the sonar equation are integrated over for a single time sample in the received intensity, and cannot be untangled using simple multiplication and division.

Synthetic aperture sonar is a wideband, nearfield imaging algorithm, and the assumption of plane wave incidence is strongly violated. For flat isotropic seafloors, the scattering cross section is also isotropic, so the nearfield imaging has little to no bias associated with scattering strength measurements. However, for steep surfaces, each receiver element along the array measured the scattered field from a different grazing angle, and can span a grazing angle interval equal to the product of the projecting and receiving transducer beamwidths. For relatively widebeam SAS systems, this means that using the sonar equation, even with the correct ensonified area, represents the average of the scattering cross section between normal incidence, and tens of degrees off normal. Since the scattering cross section can vary by tens of dB in this interval for very smooth surfaces, the scattering cross section cannot be estimated using the sonar equation with any reliability with this geometry.

Several low-frequency SAS systems are designed to image into the seafloor, enabling the detection of buried targets [4] [5] [6]. The pulse shape can be distorted from a spherical shape by refraction into the seabed and multiple reflections from subbottom interfaces. The plane wave approximation no longer is applicable. For these cases, the ensonified volume depends on seabed soundspeed contrast, pulse length, sonar geometry, and beam patterns. The received intensity represent the average of the volume scattering cross section, weighted by the incident field at various locations, and grazing angles.

Without the multiplicative relationship between measured intensity and the scattering cross section, how can the scattering cross section be estimated in these cases? A common approach is a parametric estimate, in which a model for the scattering cross section is proposed, and parameters of the model are estimated by comparing simulated times series to measured data. An overview of previous work on parametric estimates of the scattering cross section is given in Section 2. The case of interface scattering is detailed in Section 3, and an example inversion of the near-specular cross section from SAS data is given. Volume scattering data is presented in Section 4, along with a method to compute time series given the mean geoacoustic and volume scattering parameters, although no inversion is performed. Section 5 details future work.

2 PREVIOUS REASEARCH ON PARAMETRIC ESTIMATES OF THE SCATTERING CROSS SECTION

The lack of applicability for the sonar equation to estimate the scattering cross section near the specular direction has been previously studied for multibeam echosounders [7] [3] [8] [9]. These techniques all have in common the fact that a model with some parameters (empirical or physics-based) for the cross section is specified. Intensity time series are generated by the model and compared to the measured time series. Parameter estimates are found by some best fit criterion between measured data and synthetic time series. If the model time series is a linear function of the parameters, as in Jackson / Hefner, then confidence intervals of the parameter estimates, and thus the scattering cross section can be estimated using the residual error between the model and best-fit time series.

3 INTERFACE SCATTERING

For the case of a smooth surface normal to the sonar, each sample of the intensity time series or image pixel that interact with the surface is equal to a weighted average of the cross section over some finite angular range. The averaging is due to the extremely long arrays used in SAS, in addition to the intersection of the pule shape with the rough interface. This phenomenon has been studied for the case of multibeam echosounders, but the phenomenon is also present in SAS imagery.

3.1 Forward model

The problem of near specular scattering for SAS systems is examined here for the case of steep surfaces of smooth glacially abraded rock outcroppings in the Oslofjord. An empirical model was proposed that could capture the shape of the small-slope approximation [10], one of the most robust physics-based first-order scattering model. It has the advantage of having only three parameters, rather than the seven for the SSA, and is analytic, while the SSA is not given in closed form and computation requires a quadrature scheme, or some other method of numerical integration [10]. The empirical model is called the small-slope parameterization (SSP), and is given by

$$\sigma_{SSP} = \frac{\sigma_0}{\left(\chi_0^2 + \chi^2\right)^{p/2}} \tag{1}$$

Where σ_0 sets the overall level of the scattering strength curve, χ_0 sets the width of the specular peak, p sets the rate of decay of outside the specular peak, and χ is the incidence angle measured from the surface normal. To compute the pixel intensity, assume that prior to beamforming, the voltage sensed by each receiver have been corrected for spherical spreading, attenuation, vertical transducer directivity patterns, receiver sensitivity, and source strength, and is denoted by s_{ij}. Since these corrections have been applied, this quantity represents the square root of the scattering cross section at the location of the i^{th} pixel by the j^{th} receiving element times the ensonified area. Note that in some way, the sonar equation has been used to remove the transmission loss and calibration parameters from the measured voltage, but angular dependence of the directivity index and scattering cross section cannot be uncoupled. Although in reality, this quantity is weighted by the horizontal beam pattern of the transducers, these weights will be folded into the quantity w_{ij} which represents the combined effect of the horizontal transducer beampatterns and tapering applied during beamforming. The pixel intensity, I_i is related to s_{ij} and w_{ij} through the formula

$$I_i = \frac{1}{\Delta x\, \Delta y}\left(\sum_{j=1}^{N} w_{ij}\ s_{ij}\right)^2 \qquad (2)$$

where Δx is the along-track resolution of the system, and Δy is the range resolution of the system. The forward model can be formulated by setting $s = \sqrt{\sigma(\theta_{ij})}$, where θ_{ij} is the grazing angle between the surface normal of the i^{th} pixel, and the j^{th} receiver element. The local grazing angle at the pixel location is typically unknown, but can be estimated if interferometric bathymetry is available. Individual SAS image pixels are random quantities, and ensembles must be formed to estimate mean intensity. For seafloors with strongly varying topography, the local grazing angle changes from location to location, which makes it difficult to form ensembles. In this research, ensembles are formed by binning pixels based on its mean grazing angle sensed by all receivers, Θ, defined by

$$\Theta_i = \sum_{j=1}^{N} w_{ij}\theta_{ij} \qquad (3)$$

Once averaged pixel intensity is formed, the model pixel intensities can be compared to measured pixel intensities, and parameters of the scattering model are estimated such that it provides a best-fit to the data.

3.2 Inversion from SAS data

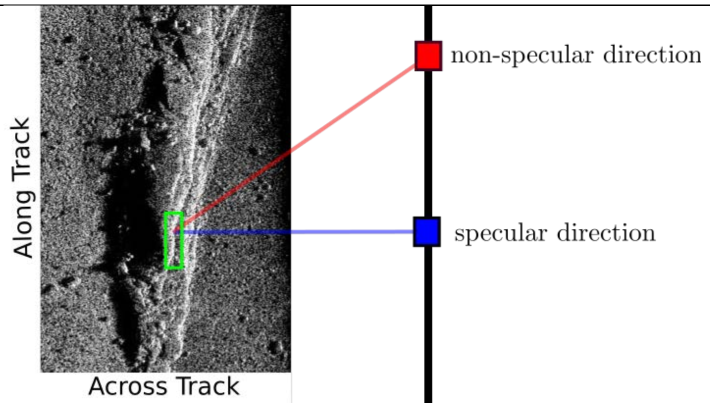

Figure 1

SAS image of rock outcrop used for near-specular scattering strength estimate. A cartoon of the synthetic array geometry is shown as a black line to the right of the SAS image, with two receiver elements displayed as red and blue. The blue receiver element faces the pixel at normal incidence and the red receiver element faces the pixel away from normal incidence. The pixel intensity is a weighted sum over the cross section at the various angles sensed by the synthetic receiver array. Horizontal image coordinates are in the across-track direction, and vertical image coordinates are in the along-track direction. The green box indicate pixels that are used to estimate the scattering cross section.

Measurements in the form of SAS iamges made in the Oslofjord, Norway near the city of Sandefjord [11]. Field data were collected in April 2011 by the Norwegian Defence Research Establishment aboard the HU Sverdrup II research vessel using the HISAS 1030 synthetic aperture sonar system. Glacially-eroded outcrops of rock called *roches moutonees* have very steep slopes on their sides, and provided an opportunity to estimate the scattering cross section near the specular direction. A SAS image of the rock outcrop is shown in Figure 1, along with the approximate location of the synthetic array shown as a black line. The rock outcrop is approximately 2m tall, and the image dimensions are 30 m in the along-track direction, and 20 m in the across-track direction. A schematic of the receiver array (not to scale) is shown to the right of the SAS image, with two elements highlighted. The blue element measures scattering from the specular direction in the bright pixels in the green box, and the red element measures scattering in away from the specular direction.

Scattering strength was estimated from the bright pixels in the green box by forming ensembles of 200 pixels each, with decreasing mean grazing angle estimated from (3). Parameters of the SSP model were estimated by using the sum of squared residuals as the objective function, and Newton's method with a line search [12]. Confidence intervals were obtained by exploring the parameter space around the best-fit solution, and finding values of the objective function which fit the set

$$\{\boldsymbol{x}_{CL}\} = \{\boldsymbol{x} | \boldsymbol{x}^T \nabla^2 f(\boldsymbol{x}^*)\boldsymbol{x} \quad \le m f(\boldsymbol{x}^*) F(m, n-m, \eta)\} \qquad (4)$$

where $\boldsymbol{x} \;\; = (\sigma_0, \chi_0, p)$ is the vector of parameters for the SSP, $\{\boldsymbol{x}_{CL}\}$ is the set of parameter vectors that fall within the confidence region, $f(\boldsymbol{x})$ is the objective function, $\boldsymbol{x}^*$is the best fit parameter vector, m is the number of model parameters (in this case $m = 3$), n is the number of data points, and $F(n, n - m, \eta)$ is the F-distribution at confidence level η, which in this case is set at 0.05. Once $\{\boldsymbol{x}_{CL}\}$ has been estimated, these parameters are used to estimate the scattering cross section at each point on the boundary of $\{\boldsymbol{x}_{CL}\}$ to determine the minimum and maximum values of the confidence interval of the scattering cross section for all grazing angles within the domain of interest. In this work, the boundary of the confidence region is computed by performing a line search in the parameter space, beginning at $\boldsymbol{x}^*$, and ending where the equality condition of (4) is met to within 1%. Note that this procedure assumes that the confidence region is convex, and that the residuals are Gaussian-distributed.

The results of the cross section inversion from pixel intensity is presented in Figure 2. Newton's method was employed with the same values for σ_0 and χ_0, but three different values of p because the steps taken in the optimization algorithm tended to change the value of p by only a few percent. A comparison of the model (with $p \approx 2.5$) and data pixel intensity, normalized such that the first sample is unity, is presented in (a). Cross section estimates and confidence regions for values of p of approximately 2, 2.5 and 3 are presented in (b). These parameter estimates differ by approximately 10 dB below 80 degrees grazing angle, and their confidence intervals are separated for the most part. This behavior indicates that the parameter space contains well-separated degenerate minima, or that the the confidence regions are non-convex. Along with estimates from SAS data, the small slope model [10] based on roughness and geoacoustic parameters. Although the cross section estimate for $p \approx 2.5$ provides the best match to the model cross section, the objective function of all three estimates are within 10 percent of one another and provide equally good fits to the data.

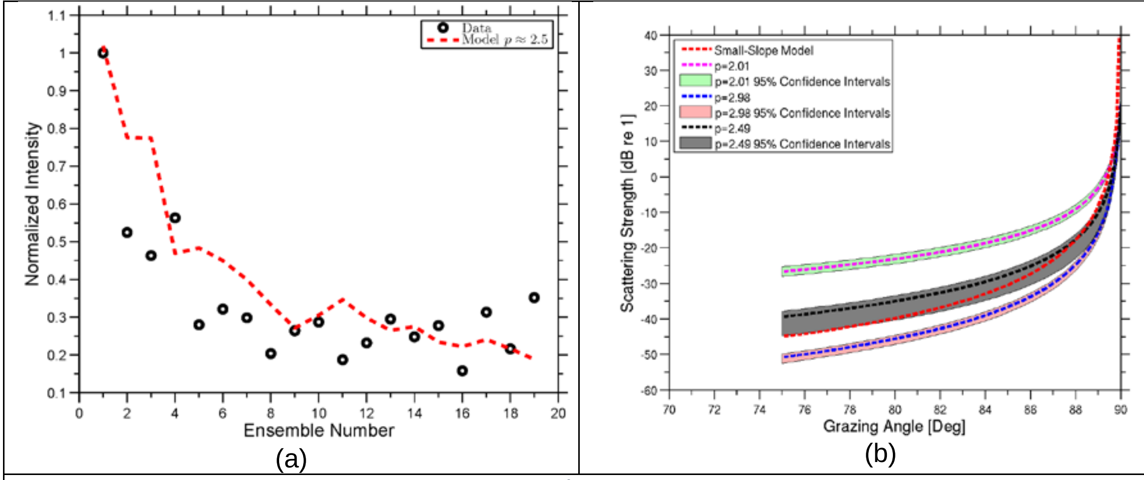

(a) (b)

Figure 2

Results from the near specular estimates. A comparison of the best-fit value of the model for pixel intensity to the data pixel intensity is given in (a). Three estimates of the scattering cross section, computed with different starting values of p are given in (b). Each results in a different estimate of the cross section, and indicates that the parameter space is degenerate.

4 VOLUME SCATTERING

Low-frequency SAS systems are typically capable of transmitting energy into the seafloor. These systems offer the potential to estimate the volume scattering cross section. Additionally, performance modelling of these systems requires an understanding of the volume reverberation levels. In this section, field data from Seneca Lake, NY data from a normal incidence system similar to a chirp sonar with 12 kHz of bandwidth centred around 18kHz will be presented. Although these data are not from a SAS system, the model detailed in this section can provide an intensity model that can used to predict target-to-background ratios for the synthetic array.

4.1 Seneca Lake Experiment.

Normal incidence backscattering data from Seneca Lake were collected in November 2014. Intensity as a function of depth and along-track position of the sonar is presented in Figure 3. The lakebed interface is at approximately 170 m depth. Below the interface, a series of closely-spaced sediment layers approximately 10 m thick is evident in the backscattered time series, and is called layer I in this research. Below this stack of layers, the intensity falls off rapidly, indicating a very low or insignificant degree of volume scattering 10 m below the water-sediment interface, which is called layer II. This pattern has been observed in chirp sonar measurements from 2-12 kHz by Halfman [13], along with a second finely layered region below the low backscatter region. They hypothesize that the finely layered sediment are muds deposited either at the terminus of the Laurentide Ice Sheet, or deposited from runoff. Layer II appears to have the same composition as Layer I, but is homogeneous. They hypothesize that some kind of turbulent sediment flow, either due to an enormous amount of subglacial fluvial discharge, or due to an avalanche of sediment built up on the steep sides. In either case, this turbulent flow destroyed any layering structure present in the top few meters of sediment, and reformed it as an isotropic layer.

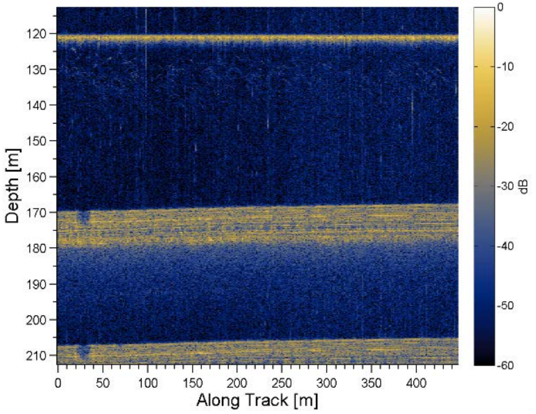

Figure 3

Backscattered intensity as a function of depth and along-track position in meters. Colorscale denotes intensity in decibels relative to an arbitrary value. Backscattering from the water column is observable abov 170 m depth, scattering finely layered medium is observable between 170 and 180 m depth, and a homogeneous region is observed below 180 m. Returns from a second closely-spaced second pulse begin at 208 m depth.

4.2 Stack of Rough layers as an equivalent heterogeneous volume

The scattering in each layer arises from different mechanisms. At these frequencies, the layer I likely causes scattering from each rough interface, and layer II could cause scattering from volume heterogeneities. Although interface scattering is likely the dominant scattering in layer I, the layers are so close together, that it is difficult to distinguish them from one another, and impossible to estimate interface scattering parameters for each one. The densely layered medium was instead modelled as an effective heterogeneous volume, as in [14]. The equivalence between a dense stack of layers and a heterogeneous volume is only true when the impedance contrast between each layer is weak, the roughness is small, and the acoustic wavelength is long compared to the layer thicknesses. For this data set, the centre wavelength of the acoustic system is 8.3 cm, and the layering in Figure 3 is on a larger scale. Treating the stack of rough interfaces as an equivalent volume would seem to be pushing the bounds of Ivakin's method, but bounds have not yet been established.

Proceeding with the equivalence of a stack of rough interfaces and a heterogeneous volume, the problem becomes predicting the intensity time series given scattering and geoacoustic parameters for each layer. The reason that we cannot simply use a form of the sonar equation is that many of the terms, especially the beam pattern, sediment attenuation, and possibly scattering cross section vary strongly within the ensonified volume. A simple calculation for a volume scattering half-space, restricted to narrow-beam systems is carried out in Appendix G of Jackson and Richardson [1], which results in an analytic expression for the intensity as a function of time in terms of decaying exponentials. For this geometry, it is advantageous to perform a general calculation that is not restricted to small angles and can handle a volume scattering layer over a volume scattering halfspace. The advantage of an analytical formula for the received intensity is lost if the small-argument approximations are not made. For convenience, the volume scattering layer will be referred to as layer I, and the semi-infinite volume scattering half space below it will be referred to as layer II.

4.3 Forward Model for scattering from a layer over a semi-infinite halfspace

For a volume scattering medium, the most general expression for the received mean square voltage is a spatial integral, similar to Eq. (G.4) in Jackson and Richardson [1],

$$\langle|V_t|^2\rangle = s_r^2 \int s_0^2 |G(r_s,r)|^2 |G(r,r_i)|^2 |b(\chi)|^2 \,\sigma_v dV \tag{5}$$

Where s_r^2 and s_0^2 are the receiver sensitivity and the source strength respectively, $G(r_s,r)$ is the Green function between the receiver location r_s and a point within the volume integral, r, $G(r,r_i)$ is the Green function between a point in the volume integral and the source location, r_i, $b(\chi)$ is the system's combined transmit and receive beam pattern and is assumed to be transversely isotropic, σ_v is the volume scattering cross section with units of m^{-1} and, and $dV = dx\,dy\,dz = r\sin\chi\, d\phi\, d\chi\, dr$ is a differential volumetric element with limits determined by the ensonified volume. The green's functions between two points in the medium are approximated in this work by ray theory, meaning that the propagation loss is represented spherical spreading, attenuation in the medium, and transmission coefficients between interfaces. Refraction effects will also be ignored. The source and receiver coordinates are assumed to be collocated at the origin in the water column. When r is in layer I, the Green functions are given by the equations,

$$|G(r,r_i)|^2 = \frac{\left|V_{wpI}\right|^2 e^{-4k_w''H/\cos\chi} e^{-4k_{pI}''(R-H/\cos\chi)}}{R^2} \tag{6}$$

$$|G(r_s,r)|^2 = \frac{\left|V_{wpI}\right|^2 e^{-4k_w''H/\cos\chi} e^{-4k_{pI}''(R-H/\cos\chi)}}{a_{\rho I}^2 R^2} \tag{7}$$

where V_{wpI} is the plane-wave reflection coefficient between the water column and layer I, and $a_{\rho I}$ is the ratio between the water density and the sediment density and layer I, k_w'' is the imaginary component of the wavenumber in water, and k_{pI}'' is the imaginary component of the wavenumber in layer I, and $R = |r_s - r| = |r - r_i|$. When r is in layer II, the Green functions are given by the equations

$$|G(r,r_i)|^2 = \frac{\left|V_{wpI}\right|^2 \left|V_{pIpII}\right|^2 e^{-2k_w''H/\cos\chi} e^{-2k_{pI}''D/\cos\chi} e^{-2k_{pII}''\left(R-\frac{H}{\cos\chi}-\frac{D}{\cos\chi}\right)}}{R^2} \tag{8}$$

$$|G(r_s,r)|^2 = \frac{\left|V_{wpI}\right|^2 \left|V_{pIpII}\right|^2 e^{-2k_w''H/\cos\chi} e^{-2k_{pI}''D/\cos\chi} e^{-2k_{pII}''\left(R-\frac{H}{\cos\chi}-\frac{D}{\cos\chi}\right)}}{a_{\rho I\rho II}^2 a_{\rho I}^2 R^2} \tag{9}$$

where D is the thickness of layer I, and k_{pII}'' is the imaginar component of the wavenumber in layer II. The pulse shape in the sediment is shown graphically in Figure 4, and divided into four cases. All cases are assumed to have azimuthal isotropy with integration limits of $\phi \in [0,2\pi]$. In case (a) the ensonified volume is a spherical section in layer I with limits $\chi \in [0, \operatorname{acos}\left(\frac{H}{r_t}\right)]$ and $r \in [\frac{H}{\cos\chi}, r_t]$. In case (b), the ensonified volume is approximated as a spherical shell with integration limits $\chi \in [0, \operatorname{acos}\left(\frac{H}{r_t}\right)]$,

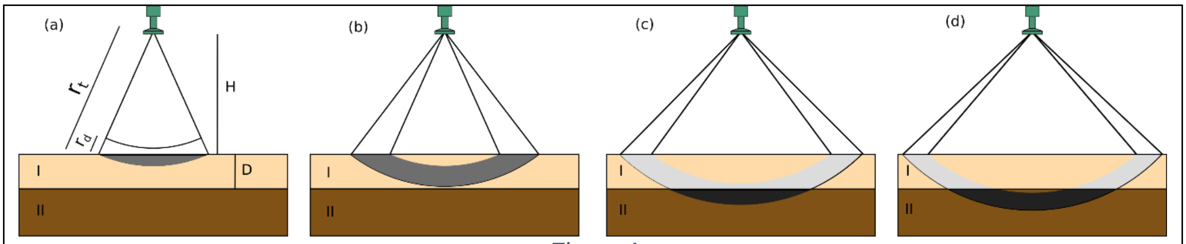

Figure 4

For a two-layer heterogeneous scattering medium, the experimental geometry, and pulse shape in each layer is shown in three shades of gray. In (a), the leading edge of the pulse is in layer I, and the trailing edge in layer II. In (b), both the leading and trailing edges of the pulse are in layer I. In (c), the leading edge is in both layers, and the trailing edge is in layer I. In (d), the leading and trailing edges of the pulse are in both layer I and layer II. The of the sonar above the interface between layer I and the water column is H, D is the thickness of layer I, rt is the range to the leading edge of the pulse, and the spatial extent of the pulse is rd.

and $r \in [r_t - r_d, r_t]$, where r_d is the range resolution of the transmitted pulse. In case (c), the ensonified volume is partially in layer I, and partially in layer II. For the layer I part, the integrals are expressed by a difference $I = I_A - I_B$, where I is the integral from (5), and integrands of I_A and I_B take on values for r in layer I. The integration limits of I_A are $\chi \in [0, \text{acos}\left(\frac{H}{r_t}\right)]$ and $r \in [r_t - r_d, r_t]$, and the integration limits of I_B are $\chi \in [0, \text{acos}\left(\frac{H+D}{r_t}\right)]$ and $r \in [\frac{D+H}{\cos\chi}, r_t]$. For case (c) in layer II, the integrands in (5) take on values for layer II, and the integration limits are $\chi \in [0, \text{acos}\left(\frac{H+D}{r_t}\right)]$ and $r \in [\frac{D+H}{\cos\chi}, r_t]$. For case (d), the ensonified volume again extends into both layer I, and layer II. Whenever r is in layer I for (d), the integration is again split into two components, $I_2 = I_{2A} - I_{2B}$. The integration limits of I_{2A} are $\chi \in [0, \text{acos}\left(\frac{H}{r_t}\right)]$ and $r \in [r_t - r_d, r_t]$, and the integration limits of I_{2B} are $\chi \in [0, \text{acos}\left(\frac{H+D}{r_t}\right)]$ and $r \in [r_t - r_d, r_t]$. For case (d) whenever r is in layer II, the integration is over the domain $\chi \in [0, \text{acos}\left(\frac{H+D}{r_t}\right)]$ and $r \in [r_t - r_d, r_t]$.

To numerically evaluate (5) in layer I and layer II, the integrands are separable between r and χ except for the scattering cross section. In general, the scattering cross section depends on angle and depth. If depth-dependence of can be ignored, then the integral over r can be computed analytically. If σ_v is assumed to be a constant, a common simplification [15], then it may be taken outside both the integral over r and over χ. The remaining angular integration can be integrated by numerical quadrature.

4.4 Inversion for volume scattering parameters.

If the volume scattering cross section is independent of angle and depth, then time series is directly proportional to σ_v and can be estimated if all other geoacoustic quantities and the geometry is known. If complete information on ground truth is not available, then an inversion for the unknown geoacoustic parameters, as well as the volume scattering cross section must be performed.

5 FUTURE WORK

The degenerate solutions in Section 3 likely result from the assumption of convexity and connectedness of the confidence region. A better understanding of the confidence region could be obtained by using statistical optimization methods, such as simulated annealing, or Monte-Carlo Markov Chain sampling [16]. Similar methods could be applied to inversion of volume scattering parameters, although the sensitivity of the received time series to the seafloor parameters should be examined first.

6 ACKNOWLEDGEMENTS

Funding for this work was provided by Office of Naval Research Grant No. N00014-13-1-0056 and Internal Research and Development funds from the Applied Research Laboratory at Pennsylvania State University.

7 REFERENCES

1. D. R. Jackson and M. D. Richardson, High-Frequency Seafloor Acoustics, New York: Springer, 2007.
2. K. Williams and D. R. Jackson, "Bistatic bottom scattering: Model, experiments and model/data comparison," *J. Acoust. Soc. Am.,* vol. 103, no. 1, pp. 169-181, 1998.
3. L. Hellequin, J. M. Boucher and X. Lurton, "Processing of high-frequency multibeam echo sounder data for seafloor characterization," *IEEE Journal of Oceaning Engineering,* vol. 28, no. 1, pp. 78-89, 2003.
4. K. L. Williams, S. G. Kargl, E. I. Thorsos, D. S. Burnett, J. L. Lopes, M. Zampolli and P. L. Marston, "Acoustic scattering from a solid aluminum cylinder in contact with a sand sediment: Measurments, modeling and interpretation," *Journal of the Acoustical Society of America,* vol. 127, no. 6, pp. 3356-3371, 2010.
5. A. J. Hunter and R. van Vossen, "Sonar target enhancement by shrinkage of incoherent wavelet coefficients," *Journal of the Acoustical Society of America,* vol. 135, no. 1, pp. 262-268, 2013.
6. A. J. Hunter, R. van Vossen, B. A. J. Quesson and A. L. D. Beckers, "Detection of Underwater UXOs in Mud," Final Report for SERDP Project MR-2200, 2013.
7. E. Pouliquen and X. Lurton, "Identification de la nature du fond de la mer à l'aide de signaux d'ècho-sondeurs. I. Modèlisation d'èchos rèverbères par le fond," *Acta Acoustica,* vol. 2, no. 3, pp. 113-126, 1994.
8. D. R. Jackson, B. T. Hefner, A. Ivakin and G. Wendelboe, "Seafloor characterisation using physics-based inversino of multibeam sonar data," in *Proceedings of the 11th European Conference on Underwater Acoustics*, Edinburgh, Scotland, 2012.
9. B. T. Hefner, D. R. Jackson, A. N. Ivakin and G. Wendelboe, "Physics-based inversion of multibeam sonar data for seafloor characterization," *Journal of the Acoustical Society of America,* vol. 134, no. 5, p. 4240, 2013.
10. R. F. Gragg, D. Wurmers and R. Gauss, "Small-slope scattering from rough elastic ocean floors: General theory and computational algorithm," *Journal of the Acoustical Society of America,* vol. 110, no. 6, pp. 2878-2901, 2001.
11. O. Midtgaard, R. E. Hansen, T. O. Saebo, V. Myers, J. R. Dubberly and I. Quidu, "Change detection using synthetic aperture sonar: preliminary results from the Larvik trial," in *Proc. IEEE OCEANS 2011*, Wikoloa, HI, 2011.
12. J. Nocedal and S. J. Wright, Numerical Optimization, New York, NY: Springer, 2006.
13. J. D. Halfman and D. T. Herrick, "Mass Movement and Reworking of Late Glacial and Postglacial Sediments in Northern Seneca Lake, New York," *Northeaster Geology and Environmental Sciences,* vol. 20, no. 3, pp. 227-241, 198.
14. A. N. Ivakin, "A unified approach to volume and roughness scattering," *Journal of the Acoustical Society of America,* vol. 103, no. 2, pp. 827-837, 1998.
15. D. R. Jackson, D. P. Winebrenner and A. Ishimaru, "Application of the composite roughness model to high-frequency bottom backscattering," *Journal of the Acoustical Society of America,* vol. 79, no. 5, pp. 1410-1422, 1986.
16. S. E. Dosso, "Quantifying uncertainty in geoacoustic inversion. I. A fast Gibbs sampler approach," *Journal of the Acoustical Society of America,* vol. 111, no. 1, pp. 129-142, 2002.